Liquidlike Cu atom diffusion in weakly ionic compounds Cu_2S and Cu_2Se

Keenan Zhuo,[1,*,†] Jing Wang,[1,†] Jianping Gao,[1] Uzi Landman,[1] and Mei-Yin Chou[1,2,‡]
[1]*School of Physics, Georgia Institute of Technology, Atlanta, Georgia, 30332-0430, USA*
[2]*Institute of Atomic and Molecular Sciences, Academia Sinica, Taipei 106, Taiwan*

(Received 8 April 2020; revised 19 June 2020; accepted 16 July 2020; published 4 August 2020)

Copper sulphide (Cu_2S) and copper selenide (Cu_2Se) are known to exist in solid (S/Se)-liquid (Cu) hybrid phases which exhibit favorable thermoelectrics properties. The diffusion characteristics and its mechanism in these systems are therefore of significant interest. In this paper, we analyze these properties through examining the atomic radial distributions, mean-square displacements, and velocity autocorrelations obtained from *ab initio* molecular dynamics simulations. Exceptionally high Cu diffusion coefficients with values over 10^{-5} cm^2/s are obtained, indicating the unexpected liquidlike behavior of Cu in these weakly ionic compounds. The diffusion mechanism obtained through analysis of the Cu atomic trajectories is found to be at variance with the previously proposed Chudley-Elliott jump diffusion model. In addition, tunability of these diffusion coefficients via small changes in the stoichiometry, namely, Cu deficiencies, is demonstrated. The higher number of low-frequency acoustic phonon modes associated with Se sublattices, compared to those with S sublattices, correlates well with the experimentally observed thermal conductivity difference between Cu_2S and Cu_2Se.

DOI: 10.1103/PhysRevB.102.064201

I. INTRODUCTION

It has long been known that superionic metal halides such as CuX and AgX (X = Cl, Br, and I) have very high cation diffusion coefficients of over 10^{-5} cm^2s^{-1} [1–3]. Such liquidlike cation diffusion rates are usually achieved at high temperatures of around 700 K [1–5], while these compounds still maintain a solid structure with the anions forming a crystalline sublattice. Recently, superionic water ice was also realized by laser-driven shock-compression experiments on water ice VII [6]. Near 5000 K at 190 GPa the ice melts, creating fast-diffusing liquidlike hydrogen ions moving within a solid lattice of oxygen atoms. This liquid-solid combination is not usually expected in weakly ionic compounds. However, recent *ab initio* molecular dynamics (MD) simulations showed that copper sulfide (Cu_2S) possesses a high Cu diffusion rate of around 2.2×10^{-6} cm^2s^{-1} in the hexagonal β phase at a relatively low temperature of 450 K [7]. This finding is supported by earlier experimental results that indicated Cu diffusion coefficients reaching over 10^{-6} cm^2s^{-1} at temperatures under 350 K [8,9]. Even though these values are still one order of magnitude smaller than the diffusion coefficient in superionic metal halides, it is a highly unusual behavior in a system that is not as strongly ionic. Previous neutron data also indicated that the closely related copper selenide Cu_2Se could have high Cu diffusion rates of the order of 10^{-5} cm^2s^{-1} at 430 K [10,11].

Cu_2S and Cu_2Se have long been considered as possible solar cell materials [12–16]. Recently, realization of the implications of their solid-liquid nature has renewed interest in these materials for other energy related applications. In fact, their solid-liquid nature makes them natural systems for phonon liquid electron crystals (PLECs), which are highly sought after as thermoelectric materials [17,18]. The thermoelectric efficiency of a material is measured by the dimensionless figure of merit $ZT = S^2\sigma T/\kappa$, where S is the Seebeck coefficient, σ is the electrical conductivity, T is the thermodynamic temperature, and κ is the total thermal conductivity. A major obstacle in the search for high ZT thermoelectric materials is the fact that S, σ, and κ are difficult to be optimized individually because they are influenced by a similar set of material properties. However, a PLEC offers more distinct electron and phonon pathways to overcome this problem. In Cu_2S and Cu_2Se, the solid sublattice of S or Se atoms provides a crystalline pathway for good electrical conduction, while the liquid Cu sublattice enhances phonon scattering which allows for unusually low thermal conductivities below $1 Wm^{-1}K^{-1}$ without overly disrupting electron transport [17,18]. In recent experiments, the ZT values of Cu_2S and Cu_2Se have been measured to be as high as 1.7 and 1.5, placing them in direct competition with some of the best thermoelectric materials known to date [17,18]. Moreover, they are cheap, abundant, and nontoxic unlike their major competitors.

Cu_2S and Cu_2Se are also of interest in high capacity rechargeable ion batteries [19–23]. In particular, there is a debate over the lithiation and delithiation mechanism in Li ion batteries with copper sulfide electrodes which may involve the formation of $Cu_{2-x}S$ as an intermediate phase [21,22]. The actual mechanism is expected to be heavily influenced by Cu and Li diffusion rates within $Cu_{2-x}S$, which necessitates an understanding of how the $Cu_{2-x}S$ structure influences cation mobilities [20–22].

Cu_2S and Cu_2Se exist in various phases, depending on temperature and composition, with their high temperature phases

*Present address: Intel Corporation, 2200 Mission College Blvd, Santa Clara, California 95054, USA.
†These two authors contributed equally.
‡mychou6@gate.sinica.edu.tw

known to be disordered. Earlier experimental studies focused primarily on their ordered room-temperature α phase [8–10], and a recent theoretical study [7] focused on the hexagonal β phase of Cu_2S at intermediate temperatures where the Cu atoms begin to exhibit liquidlike behavior. It is currently unknown how high of a diffusion rate of Cu may be achieved in the Cu_2S and Cu_2Se systems as they undergo further phase changes with increasing temperature. To this aim, we focus in this paper on the high-temperature cubic γ phase of $Cu_{2-x}S$ and the cubic β phase of $Cu_{2-x}Se$ ($x = 0$ and 0.03), which are technologically important as high ZT thermoelectric materials operating at temperatures close to 1000 K [17,18]. We note that these high-temperature phases are also expected to be more easily accessible in experiments due to their larger phase fields in comparison to other phases of $Cu_{2-x}S$ and $Cu_{2-x}Se$ [24,25].

In this paper, we theoretically study Cu atom diffusion in the high-temperature cubic phases of $Cu_{2-x}S$ and $Cu_{2-x}Se$. We perform *ab initio* MD simulations and calculate from our simulation trajectory data several characteristic properties including radial distribution functions, mean-square displacements (MSDs), and velocity autocorrelation functions (VACFs). Based on these data, we find that Cu atom diffusion coefficients are higher than 3×10^{-5} cm^2s^{-1}, indicating an unexpected liquidlike behavior in the S/Se sublattice of these weakly ionic compounds. We also examine the diffusion mechanism deduced from the atomic trajectories and find it to be inconsistent with the Chudley-Elliott (CE) jump diffusion model [26] proposed previously [10,11]. We then compare and contrast the structural and vibrational properties of $Cu_{2-x}S$ and $Cu_{2-x}Se$ so as to understand the thermal conductivity difference between $Cu_{2-x}S$ and $Cu_{2-x}Se$.

II. PHASES AND STRUCTURE OF Cu_2S AND Cu_2Se

The detailed phase diagrams of Cu_2S and Cu_2Se are given in Refs. [24,25]. At room temperature, both Cu_2S and Cu_2Se have ordered monoclinic crystal structures where all their atoms occupy fixed positions [27,28]. These are their α phases. At temperatures above 700 K and 400 K for Cu_2S and Cu_2Se, respectively, the relevant S or Se atoms adopt a face-centered-cubic (fcc) structure [28–31] while the Cu atoms become liquidlike and diffuse freely in the S or Se lattice [29,32]. These are the γ and β phases of Cu_2S and Cu_2Se, respectively. Between its monoclinic and fcc phases, Cu_2S has an additional intermediate phase where the S atoms form a hexagonal lattice [27,30,33] with the Cu atoms being liquidlike as well. This is the β phase of Cu_2S which has been studied by previous simulations [7], although the phase field for this particular hexagonal phase is very small [24]. We also note that the nomenclature for the various phases of Cu_2S and Cu_2Se is somewhat varied among different publications, for example, the γ phase $Cu_{1.8}S$ is also called digenite [34]. In what follows, we deal exclusively with the high temperature $Cu_{2-x}S$ (γ) and $Cu_{2-x}Se$ (β) phases, with both having a crystalline fcc S or Se sublattice. We will refer to these simply as the fcc phases.

In this section, we describe the structural models of Cu_2S and Cu_2Se which we use to begin our simulations, with particular reference to how we treat the Cu disorder. For Cu_2S, x-ray diffraction (XRD) has determined its lattice constant to be 5.762 Å for the cubic fcc structure at 773 K [30]. Additionally, the occupation probabilities of Cu at three different Wyckoff sites (4*b*, 8*c*, and 192*l*) were obtained in the refinement. In light of the liquid nature of the Cu atoms, we interpret these preferred sites as those which Cu atoms tend to frequently or closely pass by, in the course of their diffusion through the close-packed fcc lattice formed by the S atoms. Each of the eight Cu 8*c* sites has four nearest-neighbor S sites, which form a tetrahedral cage around it as depicted in Fig. 1(a). The 192*l* sites occur in clusters of six on each face of these tetrahedra. The eight polyhedra which the 192*l* sites form around their respective central 8*c* sites are shown in Fig. 1(c), relative to the cubic unit cell of S atoms. The single 4*b* site, not illustrated here, is at the center of the cubic unit cell.

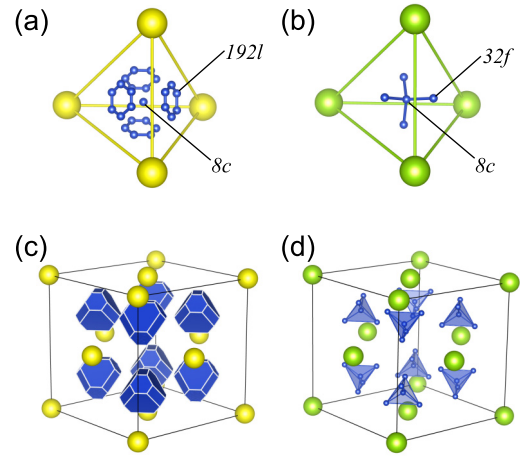

FIG. 1. (a) and (b) highlight the preferred Cu symmetry sites relative to the tetrahedron formed by closest S or Se atoms. Cu (blue spheres) atoms are shown at all preferred symmetry sites. (c) and (d) show the cubic structure of the high temperature phases of Cu_2S and Cu_2Se, respectively. S (yellow spheres) and Se (green spheres) atoms in both structures occupy fixed fcc sites. This figure was illustrated with VESTA [35].

We make use of the experimental results [30] and adopt the approach described in Ref. [34], albeit with our own slight modifications, as the starting point for creating structural models of Cu_2S. Specifically, we will ignore the 4*b* site because of its low 5% occupation probability in the x-ray structure refinement. Additionally, we insist on having exactly one Cu per interstitial region so there are no vacancies near the 8*c* sites and, consequently, Cu atoms will not be too close to each other. In our algorithm for generating a random cubic unit cell, we first choose randomly either a 192*l* or the lone 8*c* site for Cu to occupy in a particular polyhedron, according to the Cu occupation probabilities listed in Table I. If a 192*l* site is chosen, we further randomly select one out of the 24 192*l* sites on the polyhedron, all of which we assign equal probability. To simulate sufficient disorder of the Cu atoms, we use a $2 \times 2 \times 2$ cubic simulation cell with the atomic stoichiometry of $Cu_{64}S_{32}$.

We follow a similar process for generating a $2 \times 2 \times 2$ cubic simulation cell ($Cu_{64}Se_{32}$) of Cu_2Se with randomly distributed Cu atoms, based on structural parameters obtained

TABLE I. S, Se, and Cu occupation probabilities for various XRD-determined Wyckoff symmetry sites in cubic Cu_2S and Cu_2Se (Refs. [30,31]). The initial occupation in our simulations is also given.

Atom	Wyckoff site	Description	XRD Occupation (Refs. [30,31])	Initial Configurations
		Cu_2S (5.762 Å)		
S	4*a* (0, 0, 0)	Face-centered cubic	100%	100%
Cu (1)	8*c* (1/4, 1/4, 1/4)	Tetrahedral	25.75%	30%
Cu (2)	192*l* (0.11, 0.17, 0.28)	Four clusters of six sites arranged tetrahedrally around each 8*c* site	69.5%	70%
Cu (3)	4*b* (1/2, 1/2, 1/2)	Octahedral	4.75%	0%
		Cu_2Se (5.85 Å)		
Se	4*a* (0, 0, 0)	Face-centered cubic	100%	100%
Cu (1)	8*c* (1/4, 1/4, 1/4)	Tetrahedral	71.87%	70%
Cu (2)	32*f* (1/3, 1/3, 1/3)	Four sites arranged tetrahedrally around each 8*c* site	28.13%	30%

experimentally in Ref. [31]. Here, the preferred Cu sites are the 8*c* and 32*f* sites. The 32*f* sites are arranged tetrahedrally around the 8*c* site as illustrated in Fig. 1. We list our chosen structural parameters in Table I and use a lattice constant of 5.85 Å for Cu_2Se, obtained by extrapolating the temperature-dependent data from Ref. [31].

III. COMPUTATIONAL DETAILS

We first perform a random structure search to identify the most stable structures of disordered Cu_2S and Cu_2Se. Based on the structural rules outlined above, we create 20 structures having different Cu distributions each for Cu_2S and Cu_2Se. All these random configurations are structurally optimized, and the lowest energy structures for each material are considered for further analysis.

To perform structural optimizations at the experimental volume, we make use of the generalized gradient approximation [36,37] within density functional theory (DFT) with projector augmented-wave pseudopotentials [38,39]. Due to our large $2 \times 2 \times 2$ cubic simulation cell, we use a small $2 \times 2 \times 2$ k-point grid to sample the Brillouin zone and a force convergence criterion of $0.02\,\mathrm{eV\AA}^{-1}$. Our simulations are all implemented with the VIENNA AB INITIO SIMULATION PACKAGE (VASP) [40–43].

Starting with the lowest energy structures optimized at 0 K from our random structure search, we perform *ab initio* MD simulations with the Born-Oppenheimer approximation on Cu_2S and Cu_2Se to evaluate the liquidlike behavior of Cu and its interactions with the S and Se sublattices. Subsequently, we repeated the same simulations for $Cu_{1.97}S$ and $Cu_{1.97}Se$ as well, thus allowing us to explore the effect of Cu deficiencies. In the latter simulations, these structures were obtained simply by randomly removing a single Cu atom from the $Cu_{64}S_{32}$ and $Cu_{64}Se_{32}$ supercells. Our MD simulations were also performed with VASP, using similar settings as outlined for the *ab initio* random structure search method above. However, the MD simulations sample the Brillouin zone only at the Γ point. For each system, we begin the simulation at 0 K and slowly ramp up the temperature to the desired 900 K over a period of 2 ps. Subsequently, we allow our systems to equilibrate for a minimum of 50 ps. It should be noted that after the equilibration at 900 K, all copper atoms are found to have moved from their initially assigned positions to form a liquidlike medium that permeates the space between S (or Se) atoms which remain ordered about their crystalline lattice positions; in other words, following equilibration at the higher temperature the Cu atoms are not bound to lattice sites of their own. It is only after this initial equilibration period that we begin collecting data over an additional 70-ps interval. All simulation time steps are 1 fs long. Our simulations are performed using the canonical NVT ensemble (with the number of particles (N), volume (V) and temperature (T), held constant), and we employ the Nóse-Hoover thermostat [44,45]. The equations of motion are integrated using the Verlet algorithm with forces calculated from the Hellmann-Feynman theorem [46].

IV. RESULTS AND DISCUSSIONS

A. Atomic configurations and structural properties

From our MD simulations, we first compute the partial radial distribution functions $g_{\alpha\beta}(r)$ so as to characterize the structural properties of the $Cu_{2-x}S$ and $Cu_{2-x}Se$ solid-liquid hybrids. The quantity $g_{\alpha\beta}(r)$ in Eq. (1) measures the probability of finding an atom of species β separated by a distance r from species α, relative to the average number density of species β [47–49],

$$g_{\alpha\beta}(r) = \left\langle \frac{1}{N_\alpha \rho_\beta} \sum_{i=1}^{N_\alpha} \sum_{j=1}^{N_\beta} \delta(\vec{r} + \vec{r}_j - \vec{r}_i) \right\rangle, \qquad (1)$$

where N_α and ρ_α are the total number and the average number density of atomic species α, respectively. The first peak in each $g_{\alpha\beta}$ indicates the ideal separation between species α and β in the simulation. We show the partial radial distribution functions g_{SS} (g_{SeSe}), g_{CuCu} and g_{SCu} (g_{SeCu}) at 900 K in the $Cu_{2-x}S$ ($Cu_{2-x}Se$) system, where $x = 0$ and 0.03, in Figs. 2(a)–2(c), respectively. We first note that Cu vacancy defects barely change the radial distribution functions. This implies that minor Cu deficiencies are insufficient to strongly alter structural properties in the Cu_2S and Cu_2Se systems. This further indicates that large differences observed experimentally in the thermoelectric properties due to Cu deficien-

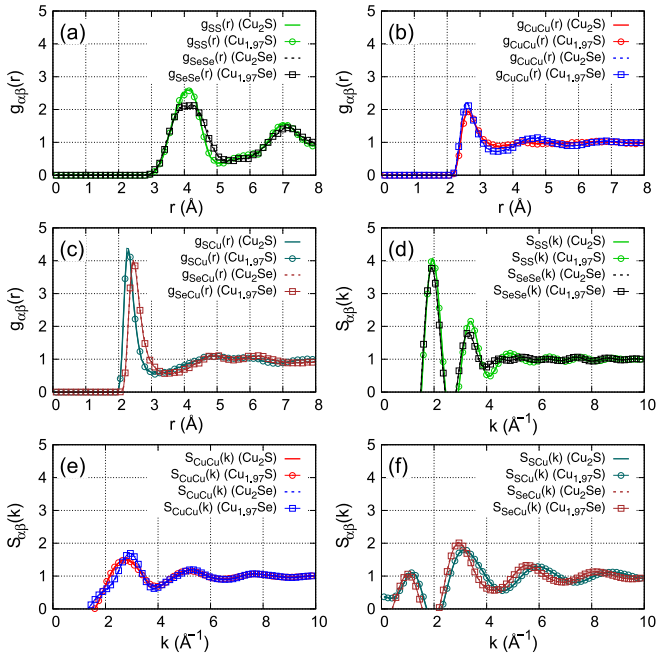

FIG. 2. Partial radial distribution functions: (a) g_{SS} (g_{SeSe}), (b) g_{CuCu}, and (c) g_{SCu} (g_{SeCu}) in $Cu_{2-x}S$ ($Cu_{2-x}Se$), where $x = 0$ and 0.03. Partial static structure factors: (d) S_{SS} (S_{SeSe}), (e) S_{CuCu} and (f) S_{SCu} (S_{SeCu}) in $Cu_{2-x}S$ ($Cu_{2-x}Se$) where $x = 0$ and 0.03. Results are obtained from *ab initio* molecular dynamics simulations at 900 K.

cies result, most likely, from other mechanisms. One possibility could be the increase in hole carrier concentration since Cu deficiencies naturally lead to *p*-type doping in $Cu_{2-x}S$ and $Cu_{2-x}Se$. This in turn leads to higher electrical and thermal conductivities as seen in experiments [17,18].

From Fig. 2(a), we also see that $g_{SS}(r)$ and $g_{SeSe}(r)$ have very distinct peaks and troughs. This is expected due to the ordered crystalline nature of the S and Se sublattices. In addition, their first peaks occur at around $r = 4.1$ Å which is the expected nearest neighbor S-S, or Se-Se, separation in the fcc lattices which we employ. The broadness of these peaks is an indication of thermal effects. Since the primary $g_{SeSe}(r)$ peak is not as sharp as that of $g_{SS}(r)$, we conclude that Se atoms typically undergo larger displacements about their mean positions. This is likely due to the larger size of Se atoms which would require them to make larger displacements as Cu atoms diffuse through the Se fcc sublattice in $Cu_{2-x}Se$.

On the other hand, $g_{CuCu}(r)$ in Fig. 2(b) along with both $g_{SCu}(r)$ and $g_{SeCu}(r)$ in Fig. 2(c) all display a single large peak which decays rapidly to unity. This indicates the fast loss of long-range order, which is characteristic of liquid behavior. Comparing the $g_{CuCu}(r)$ results, we see that $g_{CuCu}(r)$ in $Cu_{2-x}Se$ have clear small oscillations while $g_{CuCu}(r)$ in $Cu_{2-x}S$ decays smoothly to unity after the primary peak. This behavior is reasonable, considering again the larger size of Se atoms which causes significantly more Cu backscattering and hinders the Cu diffusion. The cage effect, as this is known, is thus stronger in $Cu_{2-x}Se$ than in $Cu_{2-x}S$. Of all the partial radial distribution functions in Figs. 2(a)–2(c), $g_{SCu}(r)$ and $g_{SeCu}(r)$ have the highest and sharpest peaks. This means that S-Cu and Se-Cu interactions are far more significant than S-S, Se-Se and Cu-Cu interactions. We also note that the primary peak separation of about 0.15 Å between $g_{SCu}(r)$ and $g_{SeCu}(r)$ is the greatest one among all peak separations for the two systems. Thus, the characteristic separation between Se-Cu pairs is about 5% larger than that between S-Cu pair. Again this may be attributed to the larger size of Se atoms.

TABLE II. Coordination numbers calculated from Eq.(2) between pairs of S, Se and Cu atoms in $Cu_{2-x}S$ and $Cu_{2-x}Se$ ($x = 0$ and 0.03) from *ab initio* molecular dynamics simulations at 900K.

	$N_{SS/SeSe}$	$N_{(S/Se)Cu}$	$N_{Cu(S/Se)}$	N_{CuCu}
Cu_2S	12.0	6.1	3.1	7.0
$Cu_{1.97}S$	12.1	6.0	3.1	6.9
Cu_2Se	12.5	8.1	4.0	6.1
$Cu_{1.97}Se$	12.6	7.7	4.0	6.0

Integrating $g_{\alpha\beta}(r)$ yields an estimate of the coordination number $N_{\alpha\beta}$ [49],

$$N_{\alpha\beta} = \int_0^{r_{\min}} 4\pi r^2 g_{\alpha\beta}(r)\rho_\beta dr, \tag{2}$$

where $r_{\min}$ is the first minimum of $g_{\alpha\beta}(r)$. The coordination numbers $N_{\alpha\beta}$ for all cases are listed in Table II. Comparing the coordination numbers for $Cu_{2-x}S$ and $Cu_{2-x}Se$, we note that in all cases S (Se) atoms are coordinated to about 12 other S (Se) atoms on average. This is as expected from the fcc sublattice formed by S (Se), since 12 is the number of nearest-neighbors for each atom in an ideal FCC lattice. The coordination numbers involving Se and Cu pairs are significantly more than those involving S and Cu pairs. In fact, for the case of $Cu_{2-x}Se$, N_{SeCu} and N_{CuSe} are around 8.0 and 4.0, respectively, implying that the Cu atoms are ideally close to the tetrahedral sites. As for $Cu_{2-x}S$, $N_{CuS} = 3.1$ suggests that Cu atoms are located closer to the faces of the tetrahedral cages. This naturally brings Cu atoms closer together in $Cu_{2-x}S$ such that N_{CuCu} in $Cu_{2-x}S$ is larger than that in $Cu_{2-x}Se$. These observations are likely consequences of the aforementioned cage effect. In contrast, in $Cu_{2-x}Se$, the larger Se atoms keep Cu atoms more confined within tetrahedral cages, which simultaneously allows more Se atoms to share a similar set of Cu neighbors.

The partial radial distribution functions may further be Fourier transformed to obtain the partial static structure factors $S_{\alpha\beta}(k)$ which are experimentally measurable via x-ray or neutron scattering. Since $g_{\alpha\beta}(r)$ depends only on the magnitude of the interatomic separations r, the Fourier transform of $g_{\alpha\beta}(r)$ simplifies to the relation [48]

$$S_{\alpha\beta}(k) = 1 + 4\pi\rho_\beta \int \frac{\sin(kr) g_{\alpha\beta}(r)}{kr} r^2 dr. \tag{3}$$

In all cases, the maximum range of r is limited to half our simulation cell size, which places a lower bound on k, below which $S_{\alpha\beta}(k)$ are not reliable. We estimate this lower bound to be around 1 Å^{-1}. Figures 2(d)–2(f), respectively, show the partial static structure factors S_{SS} (S_{SeSe}), S_{CuCu}, and S_{SCu} (S_{SeCu}) in $Cu_{2-x}S$ ($Cu_{2-x}Se$), where $x = 0$ and 0.03.

The total radial distribution functions are obtained by summing the relevant partial radial distribution functions

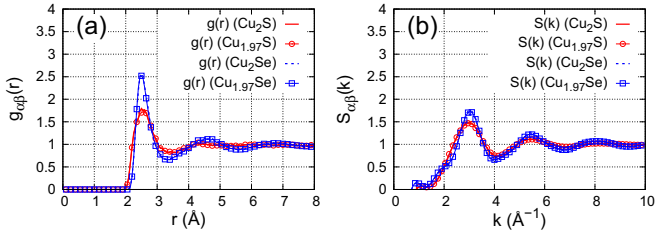

FIG. 3. (a) Total radial distribution functions $g(r)$ and (b) total static structure factors $S(k)$ of $Cu_{2-x}S$ and $Cu_{2-x}Se$ ($x = 0$ and 0.03) from *ab initio* molecular dynamics simulations at 900 K.

with the appropriate weighting according to the Faber-Ziman formalism [50]

$$g(r) = \frac{\sum_{\alpha,\beta} x_\alpha x_\beta b_\alpha b_\beta g_{\alpha\beta}(r)}{\sum_{\alpha,\beta} x_\alpha x_\beta b_\alpha b_\beta}, \tag{4}$$

where x_α is the molar fraction, and b_α is the scattering amplitude for species α. To make our results relevant to neutron-scattering experiments, we choose to use neutron-scattering lengths as b_α. From Ref. [51], these are 2.847 fm, 7.970 fm, and 7.718 fm for S, Se, and Cu, respectively. The total radial distribution functions are displayed in Fig. 3 along with the total static structure factor $S(k)$ obtained by Fourier transforming the $g(r)$ functions. They most strongly resemble the $g_{\mathrm{CuCu}}(r)$ and $S_{\mathrm{CuCu}}(k)$ functions owing to the large molar fraction and neutron scattering lengths of Cu. Experimental neutron-scattering data on cubic $Cu_{1.75}Se$ at 430 K includes peaks at 3 $Å^{-1}$, 5.5 $Å^{-1}$ and 8 $Å^{-1}$ [10]. Figure 3(b) shows peaks at similar positions in our theoretically calculated $S(k)$ for $Cu_{2-x}Se$ ($x = 0$ and 0.03). This good agreement between theory and experiment is seen despite the much lower experimental temperature of 430 K and the considerably higher amount of Cu deficiency in $Cu_{1.75}S$.

B. Analysis of Cu Atom Diffusion

To evaluate the diffusion coefficients, we next calculate the MSD [47],

$$\langle \Delta r_\alpha(t)^2 \rangle = \left\langle \frac{1}{N_\alpha} \sum_{i=1}^{N_\alpha} |\vec{r}_i(t) - \vec{r}_i(0)|^2 \right\rangle, \tag{5}$$

of each species α. For the Cu_{2-x}s and $Cu_{2-x}Se$ systems, we show the MSDs of S and Se in Figs. 4(a) and 4(b), respectively as a function of simulation time. We see in these diagrams that the MSDs for S and Se atoms do not grow with time, and this indicates that S and Se exhibit no diffusive motion. This is in accordance with the expectation that they only vibrate about their crystalline fcc sites.

The MSDs of Cu in $Cu_{2-x}S$ are shown in Fig 4(c), and those of Cu in $Cu_{2-x}Se$ are shown in Fig. 4(d). In both diagrams, we see that Cu atoms diffuse quite significantly as evidenced by their linearly increasing MSDs. The gradient (slope) of each best-fit line is directly proportional to the diffusion coefficient [47],

$$D_{\mathrm{MSD}} = \frac{\partial}{\partial t} \langle \Delta r^2(t) \rangle / (2N_{\mathrm{dim}}), \tag{6}$$

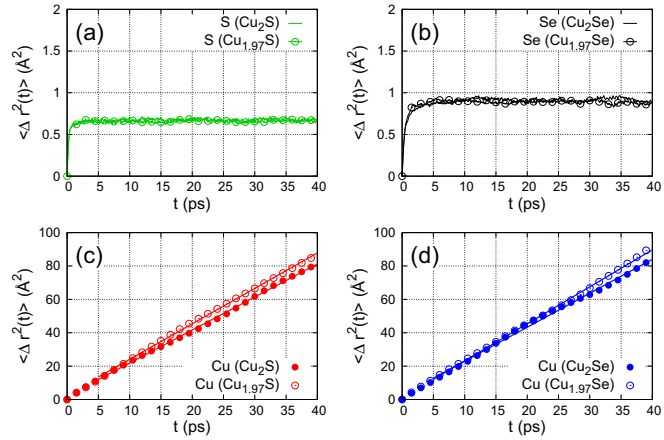

FIG. 4. Mean-square displacements $\langle \Delta r^2(t) \rangle$ of (a) S in $Cu_{2-x}S$, (b) Se in $Cu_{2-x}Se$, (c) Cu in $Cu_{2-x}S$, and (d) Cu in $Cu_{2-x}Se$ as a function of time from *ab initio* molecular dynamics simulations at 900 K. Note the scale differences between the top and bottom panels. In (c) and (d), the best linear fits are indicated by solid lines.

where $N_{\mathrm{dim}} = 3$ is the number of dimensions in the system [47–49]. In performing the straight-line fit and calculating each gradient, we only use data between 5 ps and 40 ps in the MSD graphs of Figs. 4(c) and 4(d). We list the calculated diffusion coefficients for Cu atoms in Table III. In all cases, they are of the order 10^{-5} cm^2s^{-1}, which is highly significant because this value is comparable to that in most liquids. The D_{MSD} calculated here are also an order of magnitude greater than that estimated for the hexagonal phase of Cu_2S which exists at around 450 K [7]. In addition, we observe that Cu deficiencies play an important role in tuning the diffusion coefficients D_{MSD}. Namely, Cu deficiencies consistently increase the Cu diffusion rate in both $Cu_{2-x}S$ and $Cu_{2-x}Se$ ($x = 0.03$) by around 5% or more. This is reasonable because Cu deficiencies allow S or Se atoms to be displaced more easily for the remaining Cu atoms to move through.

The VACF is another quantity which reveals important information about the underlying dynamical processes within the system studied. The normalized VACF for a certain species α is given by [52]

$$Z_\alpha(\tau) = \frac{\langle \vec{v}_\alpha(0) \cdot \vec{v}_\alpha(\tau) \rangle}{\langle \vec{v}_\alpha(0) \cdot \vec{v}_\alpha(0) \rangle}, \tag{7}$$

where τ is the time delay between the recorded velocities. We show our $Z_\alpha(\tau)$ plots in Fig. 5. Integrating the VACF is also an alternative method for calculating the diffusion coefficient

TABLE III. Cu Diffusion coefficients in $Cu_{2-x}S$ and $Cu_{2-x}Se$ calculated using the mean square displacements (D_{MSD}) and velocity autocorrelation functions (D_{VACF}) obtained from *ab initio* molecular dynamics simulations at 900 K.

	D_{MSD} (10^{-5} cm^2s^{-1})	D_{VACF} (10^{-5} cm^2s^{-1})
Cu_2S	3.3	3.5
$Cu_{1.97}S$	3.5	3.6
Cu_2Se	3.4	3.4
$Cu_{1.97}Se$	3.7	4.1

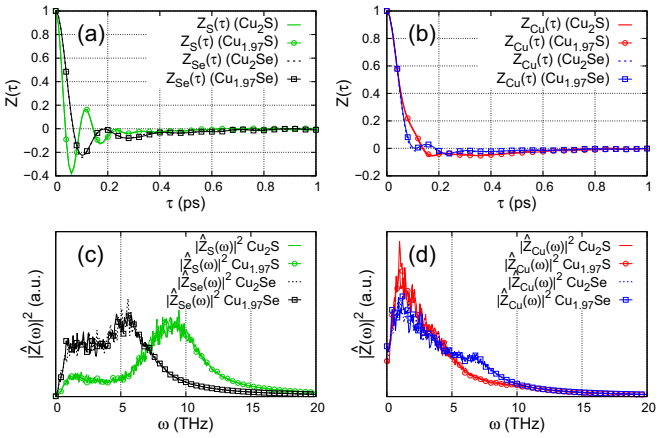

FIG. 5. Normalized velocity autocorrelation functions of (a) S/Se and (b) Cu in $Cu_{2-x}S$ and $Cu_{2-x}Se$ ($x = 0$ and 0.03). Power spectra of (c) S/Se and (d) Cu in $Cu_{2-x}S$ and $Cu_{2-x}Se$ ($x = 0$ and 0.03), obtained by Fourier transforming the velocity autocorrelation functions in (a) and (b) respectively. Each velocity autocorrelation functions is normalized by its respective value at $\tau = 0$, while each power spectrum is normalized by its respective area. Results shown here are obtained from *ab initio* molecular dynamics simulations at 900 K. Error bars are too small to be distinguished.

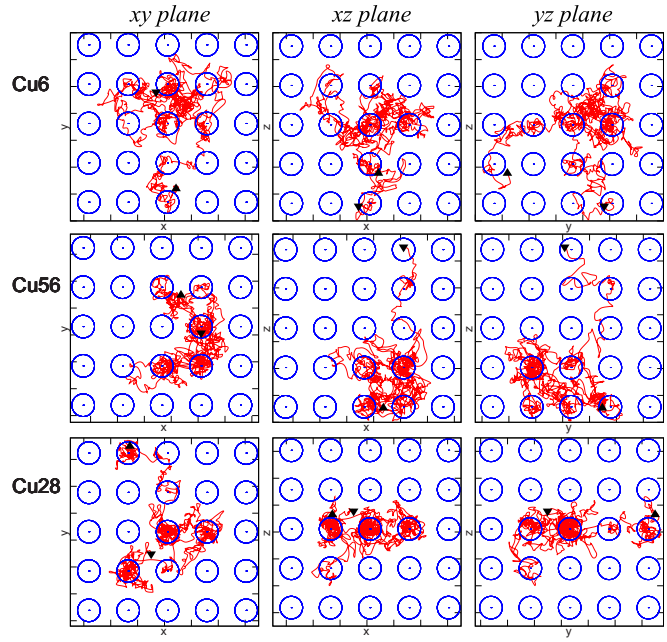

FIG. 6. Trajectories (red lines) of three representative Cu atoms in $Cu_{1.97}Se$ shown in three planar projections for the simulation run of 70 ps. The blue circles indicate the spheres tangential to the faces of the tetrahedral cages formed by fcc Se, with a diameter of 1.68 A and centered at 8*c* sites. The solid regular (inverted) triangles indicate the beginning (ending) locations of the Cu atoms.

of Cu. We refer to the diffusion coefficient calculated this way as $D_{\mathrm{VACF}} = \int d\tau \langle \vec{v}(\tau) \cdot \vec{v}(0) \rangle$ [49]. This provides a good consistency check for diffusion coefficients calculated using the MSD method. The VACF is typically a slow decaying function and calculating D_{VACF} requires a substantial integration over the time interval. We find that an integration range over the delay time τ from 0 ps to 20 ps is sufficient to provide a good level of convergence. Our calculated values of D_{VACF} listed in Table III compare favorably with D_{MSD} and display the same trends as discussed in the previous paragraph, namely, comparable diffusion coefficients for Cu in $Cu_{2-x}S$ and $Cu_{2-x}Se$ and a slight increase in the presence of Cu vacancies.

The VACFs yield further information about the solid-liquid hybrid nature of $Cu_{2-x}S$ and $Cu_{2-x}Se$. In $Cu_{2-x}S$, the VACF of S atoms [Fig. 5(a), green curve] clearly exhibits the damped harmonic motion associated with a regular solid lattice. On the other hand, the VACF of the Cu atoms [Fig. 5(b), red curve] displays a single heavily damped oscillation. This is indicative of diffusive motion associated with a liquidlike behavior. In the case of $Cu_{2-x}Se$, the VACF of Se atoms [Fig. 5(a), black curve] is also oscillatory in nature but is more heavily damped than that of S atoms [Fig. 5(a), green curve] in $Cu_{2-x}S$, owing to the greater mass of Se atoms. The VACF of Cu atoms [Fig. 5(b), blue curve] in $Cu_{2-x}Se$ exhibits a decay accompanied by weak oscillations. This is a sign of the cage effect, where Cu atoms rebound from a cage formed by the neighboring Se atoms. The calculated VACFs in Figs. 5(a) and 5(b) show little changes in the presence of Cu vacancy defects.

To understand the diffusion mechanism of Cu atoms, we examine the MD trajectories of individual Cu atoms in $Cu_{1.97}Se$ as an example. Danilkin *et al.* [10,11] proposed a CE jump diffusion model [26] for these systems with the residence time and jump length fitted to the neutron-scattering data. To check if this model describes Cu diffusion properly, we define a sphere tangential to the faces of the tetrahedral cage formed by fcc Se, centered at an 8*c* site. The diameter is about 1.68 A, as shown by blue circles in Fig. 6. According to the CE model, Cu atoms will stay within these tangential spheres most of the time and swiftly hop between them. As examples, we plot in Fig. 6 the trajectories of three Cu atoms in three different planar projections for the full simulation run of 70 ps. The solid regular (inverted) triangles indicate the beginning (ending) locations. Two of the depicted representative trajectories (marked as Cu6 and Cu56) in Fig. 6 show that the Cu atoms are essentially free from the 8*c*-site confinement, as indicated by the observation that a large portion of the particles' trajectories (red lines in Fig. 6) lie well outside the 8*c* confining regions (marked by the blue circles). The trajectory of the third representative atom (marked as Cu28 in Fig. 6) is of a more confined character but nevertheless it exhibits frequent excursion to the intersite (free) regions. Indeed, our trajectory data shows that, on average, Cu atoms spend only 30.4% out of the 70 ps time range of the MD simulation inside the tangential spheres prescribing the 8*c* confinement-sites. For the three representative atoms in Fig. 6, the atom labeled as Cu6 spends about 19% (the lowest) of the 70 ps simulation period at the confinement site, Cu56 spends about 30% (the average), and Cu54 about 42% (the highest confinement-site residence time among these selected representative Cu atoms). Such analysis revealed that the high-temperature equilibrium dynamics of the Cu atoms is dominated by diffusive trajectories which are found in the interconfinement-site (8*c*) regions, indicating that the Cu atoms are mostly meandering diffusively in the

intersite (free) regions, rather than staying for longer periods in the vicinity of the confining sites with their residence there interrupted occasionally by fast intersite hops.

In light of the above, we conclude that our findings do not conform with the above-noted CE model assumption, where the time fraction associated with the jumps between selected sites is taken to be small compared to the trapping (residence)-period at the confinement site. Consequently, our simulation data do not support the CE model as the proper description of Cu diffusion in $Cu_{1.97}Se$. Additionally, the liquid nature of the Cu atoms under the conditions considered here is manifest in relatively fast configurational structural relaxations, thus precluding consideration of a vacancy-assisted diffusion mechanism often invoked in analysis of diffusion in crystalline as well as disordered or amorphous solids. Considering the clear linearity of the Cu atoms' MSDs in Fig. 4(d), we conclude that the diffusion mechanism of Cu atoms in fcc $Cu_{1.97}Se$ is close to a normal random-walk diffusion, with some preference for Cu atom visitation in the neighborhood of the 8*c* sites.

C. Analysis of vibrations and charge transfer

The Fourier transform of the VACF yields the power spectrum [49]

$$\hat{Z}_\alpha(\omega) = \frac{1}{\sqrt{2\pi}} \int d\tau e^{i\omega\tau} Z_\alpha(\tau), \tag{8}$$

which, by construction, is proportional to the partial phonon density of states (DOS). We show these power spectra in Figs. 5(c) and 5(d) as well. Thermal conduction is expected to occur mainly through the ordered S and Se fcc sublattices via the more dispersive acoustic modes. The first peak in the $\hat{Z}_\alpha(\omega)$ should correspond to the peak in the acoustic phonon DOS. Since we see that $\hat{Z}_{Se}(\omega)$ [Fig. 5(c), black curve], has a much larger first peak than $\hat{Z}_S(\omega)$ [Fig. 5(c), green curve], we conclude that there are more acoustic phonon modes available for heat transfer in $Cu_{2-x}Se$, which correlates well with the observed significantly larger thermal conductivity of $Cu_{2-x}Se$ than that of $Cu_{2-x}S$ [17,18]. Generally, we predict that the Se sublattice transmits significantly more low frequency phonon modes in comparison to the S sublattice. Because the phonon frequencies are inversely proportional to atomic masses, this is indeed expected since the Se atom is heavier than the S one.

As for the $\hat{Z}_{Cu}(\omega)$ displayed in Fig. 5(d), we notice that these power spectra do not vanish at zero frequency. This is another signature of liquid behavior as liquids are known to possess frequency independent diffusive modes. In fact, the zero-frequency spectrum $\hat{Z}_{Cu}(0)$ gives a measure of the diffusivity in the system [53]. Nevertheless, differences here have minimal effect on the total thermal conductivity due to the solid lattices being far more effective for thermal transport.

We further compare the power spectrum of $Cu_{2-x}S$ with the partial phonon DOS of the monoclinic α phase of Cu_2S as depicted in Fig. 7. The phonon DOS of monoclinic Cu_2S [27] is obtained by calculating atomic force constants in VASP, which are then passed to the PHONOPY code [54] for a solution of the phonon dynamical matrix. The VASP calculation mentioned here utilizes a single large unit cell of monoclinic Cu_2S (96 Cu atoms and 48 S atoms), and force constants are evaluated from density-functional perturbation theory. Recall

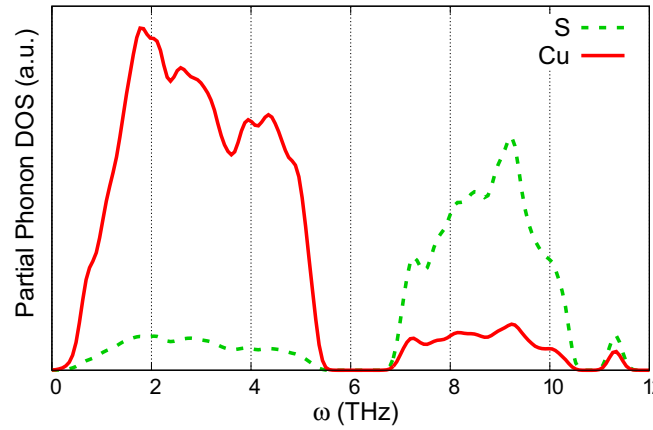

FIG. 7. Partial phonon density of states (DOS) of monoclinic Cu_2S.

that the monoclinic α phase of Cu_2S is crystalline and exists at room temperature [27]. From Fig. 7, we see that the major phonon DOS peaks of Cu and S occur in different energy ranges with a distinct energy gap in between. This implies that Cu and S phonons are already largely decoupled in the low-temperature monoclinic phase of Cu_2S, and it facilitates the partial melting of the Cu sublattice as temperature increases. In addition, we note that the Cu and S peaks in the phonon DOS of monoclinic Cu_2S occur at around 2 THz and 9 THz, respectively. In comparison, the power spectrum $\hat{Z}_S(\omega)$ in $Cu_{2-x}S$ ($x = 0$ and 0.03) also has a broad peak around 9 THz in Fig. 5(c), while the power spectrum $\hat{Z}_{Cu}(\omega)$ in Fig. 5(d) exhibits a long tail as the frequency increases. In closing our discussion about the vibrational spectra, we note here that our simulations were all carried out at sufficiently high temperatures, where the Cu atoms are found to exhibit clear liquidlike behavior. It would be of interest to explore in future studies the "melting" process of the Cu atoms in $Cu_{2-x}S$ and $Cu_{2-x}Se$, at lower temperatures than the one used by us here, including possible soft-mode development, and the transition of the Cu atoms from a highly anharmonic solid phase to the liquidlike phase discussed in this paper.

To estimate the average charge on Cu, S, and Se atoms in $Cu_{2-x}S$ and $Cu_{2-x}Se$, we perform Bader charge analysis [55–57]. The Bader charge gives the number of electrons N_α about each of the atoms of species α. The excess or deficiency in the number of electrons around atoms of species α, ΔN_α, is given by $\Delta N_\alpha = N_\alpha - N_v^\alpha$ where N_v^α is the number of valence electrons of species α included in the DFT calculations; hence $N_v^{S/Se} = 6$ and $N_v^{Cu} = 11$. The Bader charge is defined as $\Delta Q_\alpha = -\Delta N_\alpha$. Table IV shows $\Delta N_{S/Se/Cu}$ and $N_{S/Se/Cu}$ of $Cu_{2-x}S$ and $Cu_{2-x}Se$ ($x = 0$ and 0.03), each averaged over configurations obtained every 5 ps from the respective 50 ps MD simulations at 900 K. From Table IV, we see that Cu atoms donate 0.4 electrons on average to S atoms in $Cu_{2-x}S$ but this shrinks to 0.3 in the case of $Cu_{2-x}Se$. As such, $Cu_{2-x}S$ is slightly more ionic than $Cu_{2-x}Se$. Nevertheless, both materials are weakly ionic in nature.

TABLE IV. Excess electrons ($\Delta N_{S/Se/Cu}$) and number of electrons ($N_{S/Se/Cu}$), as calculated by Bader charge analysis, on S, Se, and Cu atoms in $Cu_{2-x}S$ and $Cu_{2-x}Se$ ($x = 0, 0.03$) from *ab initio* molecular dynamics simulations at 900 K.

	Cu_2S	$Cu_{1.97}S$	Cu_2Se	$Cu_{1.97}Se$
$\Delta N_{S/Se}$	0.78	0.78	0.54	0.54
ΔN_{Cu}	−0.39	−0.39	−0.27	−0.28
$N_{S/Se}$	6.78	6.78	6.54	6.54
N_{Cu}	10.61	10.61	10.73	10.72

V. CONCLUSION

We have performed *ab initio* MD simulations for the high-temperature cubic phase of $Cu_{2-x}S$ and $Cu_{2-x}Se$ ($x = 0$ and 0.03) at 900 K. Analysis of simulation data reveals that the S/Se atoms merely vibrate around their fcc lattice sites, as indicated by the almost constant MSDs in time and the regular damped oscillations in the VACFs. In contrast, the Cu atoms are found to exhibit highly uncorrelated diffusive motion within the S/Se sublattice, with linearly increasing (in time) MSDs and heavily damped VACFs. We estimate the Cu atom diffusion coefficients by using both the slope of the time-dependent MSDs and the time-integrated VACFs. Both values are consistent and are in the range of 3-4 $\times 10^{-5}$ cm^2/s, comparable to the diffusion coefficients in many liquids and an order of magnitude higher than that previously calculated for the hexagonal phase of $Cu_{2-x}S$ at 450 K. This confirms the existence of liquidlike Cu atoms and the nature of solid-liquid hybrids in these compounds. The simulation trajectories also indicate that Cu atom diffusion does not follow the CE jump diffusion model.

Comparing the S and Se power spectra obtained by Fourier transforming their respective VACFs, we find that the Se sublattice transmits more low-frequency phonons, which usually have high group velocities. This correlates well with the experimental observation that $Cu_{2-x}Se$ has a higher thermal conductivity than $Cu_{2-x}S$. Overall, Cu deficiencies do not affect structural properties significantly. However, they can increase the Cu diffusion rates in Cu_2S and Cu_2Se by around 5% or more. Finally, Bader charge analysis reveals that $Cu_{2-x}S$ and $Cu_{2-x}Se$ are only weakly ionic. This distinguishes them from the related and more well-known superionic states of matter. The highly unusual properties of solid-liquid hybrid Cu_2S and Cu_2Se, particularly a low thermal conductivity, make them attractive thermoelectric materials.

ACKNOWLEDGMENTS

We gratefully acknowledge helpful discussions with Drs. Cheng-Rong Hsing, Ching-Ming Wei, Kuei-Hsien Chen, and Lian-Ming Lyu. K.Z. is thankful for the hospitality provided by Academia Sinica where some of the calculations were performed. M.Y.C. acknowledges support from Academia Sinica under Grant No. AS-SS-109-01, and U.L. acknowledges support from the Air Force Office of Scientific Research (AFOSR), Grant No. FA9550-15-1-0519. This research used resources of the National Energy Research Scientific Computing Center (NERSC), a U.S. Department of Energy Office of Science User Facility operated under Contract No. DE-AC02-05CH11231.

[1] J. X. M. Zheng-Johansson, K. Sköld, and J. E. Jorgensen, Solid State Ionics **70**, 522 (1994).
[2] A. Kvist and R. Tärneberg, Z. für Naturforsch A **25**, 257 (1970).
[3] R. J. Friauf, J. Phys. (Paris) **38**, 1077 (1977).
[4] J. X. M. Zheng-Johansson and K. Sköld, J. Solid State Chem. **98**, 263 (1992).
[5] J. X. M. Zheng-Johansson, K. Sköld, and J. E. Jorgensen, Solid State Ionics **50**, 247 (1992).
[6] M. Millot, S. Hamel, J. R. Rygg, P. M. Celliers, G. W. Collins, F. Coppari, D. E. Fratanduono, R. Jeanloz, D. C. Swift, and J. H. Eggert, Nat. Phys. **14**, 297 (2018).
[7] L. W. Wang, Phys. Rev. Lett. **108**, 085703 (2012).
[8] U. Tinter and H. D. Wiemhöffer, Solid State Ionics **9-10**, 1213 (1983).
[9] H. Rickert and H. D. Wiemhöffer, Solid State Ionics **11**, 257 (1983).
[10] S. A. Danilkin, M. Avdeev, T.Sakuma, R. Macquart, C. D. Ling, M. Rusina, and Z. Izaola, Ionics **17**, 75 (2011).
[11] S. A. Danilkin, M. Avdeev, M. Sale, and T. Sakuma, Solid State Ionics **225**, 190 (2012).
[12] C. F. Pan, S. M. Niu, Y. Ding, L. Dong, R. M. Yu, Y. Liu, G. Zhu, and Z. L. Wang, Nano Lett. **12**, 3302 (2012).
[13] J. G. Radich, R. Dwyer, and P. V. Kamat, J. Phys. Chem. Lett. **2**, 2453 (2011).
[14] Y. Jian, X. Zhang, Q. Q. Ge, B. B. Yu, Y. G. Zhou, W. J. Jiang, W. G. Song, L. J. Wan, and J. S. Hu, Nano Lett. **14**, 365 (2014).
[15] H. Komaki, M. Iioka, A. Yamada, S. Furue, S. Ishizuka, K. Matsubara, H. Shibata, and S. Niki, Jpn. J. Appl. Phys. **51**, 10NC04 (2012).
[16] S. C. Riha, D. C. Johnson, and A. L. Prieto, J. Am. Chem. Soc. **133**, 1383 (2011).
[17] H. Liu, X. Shi, F. Xu, L. Zhang, W. Zhang, L. Chen, Q. Li, C. Uher, T. Day, and G. J. Snyder, Nat. Mater. **11**, 422 (2012).
[18] Y. He, T. Day, T. S. Zhang, H. L. Liu, L. D. Chen, and G. J. Snyder, Adv. Mater. **26**, 3974 (2014).
[19] Y. Zhao and C. Burda, Energy Environ. Sci. **5**, 5564 (2012).
[20] B. Jache, B. Mogwitz, F. Klein, and P. Adelhelm, J. Power Sources **247**, 703 (2014).
[21] A. Debart, L. Dupont, R. Patrice, and J. M. Tarascon, Solid State Sci. **8**, 640 (2006).
[22] X. H. Rui, H. T. Tan, and Q. Y. Yan, Nanoscale **6**, 9889 (2014).
[23] J. L. Yue, Q. Sun, and Z. W. Fu, Chem. Commun. **49**, 5868 (2013).
[24] D. J. Chakrabarti and D. E. Laughlin, Bull. Alloy Phase Diagrams **4**, 254 (1983).
[25] D. J. Chakrabarti and D. E. Laughlin, Bull. Alloy Phase Diagrams **2**, 305 (1981).

[26] C. Chudley and R. Elliott, Proc. Phys. Soc. London **77**, 353 (1961).
[27] H. T. Evans, Z. Kristallogr. **150**, 299 (1979).
[28] N. Frangis, C. Manolikas, and S. Amelinckx, Phys. Status Solidi A **126**, 9 (1991).
[29] M. Olivera, R. K. McMullan, and B. J. Wuensch, Solid State Ionics **28**, 1332 (1988).
[30] G. Will, E. Hinze, and A. R. M. Abdelrahman, Eur. J. Mineral. **14**, 591 (2002).
[31] A. N. Skomorokhov, D. M. Trots, M. Knapp, N. N. Bickulova, and H. Feuss, J. Alloys Compd. **421**, 64 (2006).
[32] E. Hirahara, J. Phys. Soc. Jpn. **6**, 422 (1951).
[33] M. J. Buerger and B. J. Wuensch, Science **141**, 276 (1963).
[34] P. Lukashev, W. R. L. Lambrecht, T. Kotani, and M. van Schilfgaarde, Phys. Rev. B **76**, 195202 (2007).
[35] K. Momma and F. Izumi, J. Appl. Crystallogr. **44**, 1272 (2011).
[36] J. P. Perdew, J. A. Chevary, S. H. Vosko, K. A. Jackson, M. R. Pederson, D. J. Singh, and C. Fiolhais, Phys. Rev. B **46**, 6671 (1992).
[37] J. P. Perdew, J. A. Chevary, S. H. Vosko, K. A. Jackson, M. R. Pederson, D. J. Singh, and C. Fiolhais, Phys. Rev. B **48**, 4978 (1993).
[38] P. E. Blochl, Phys. Rev. B **50**, 17953 (1994).
[39] G. Kresse and D. Joubert, Phys. Rev. B **59**, 1758 (1999).
[40] G. Kresse and J. Hafner, Phys. Rev. B **47**, 558 (1993).
[41] G. Kresse and J. Hafner, Phys. Rev. B **49**, 14251 (1994).
[42] G. Kresse and J. Furthmüller, Comput. Mater. Sci. **6**, 15 (1996).
[43] G. Kresse and J. Furthmüller, Phys. Rev. B **54**, 11169 (1996).
[44] S. Nóse, J. Chem. Phys. **81**, 511 (1984).
[45] W. G. Hoover, Phys. Rev. A **31**, 1695 (1985).
[46] L. Verlet, Phys. Rev. **159**, 98 (1967).
[47] B. Smit and D. Frenkel, *Understanding Molecular Simulations* (Academic Press, New York, 1996).
[48] M. P. Allen and D. J. Tildesley, *Computer Simulation of Liquids* (Clarendon, Oxford, 1987).
[49] J. P. Hansen and I. R. McDonald, *Theory of Simple Liquids: With Applications to Soft Matter* (Academic Press, Amsterdam, Boston, 2013).
[50] T. E. Faber and J. M. Ziman, Philos. Mag. **11**, 153 (1965).
[51] V. F. Sears, Neutron News **3**, 26 (1992).
[52] A. M. Ovrutsky, A. S. Prokhoda, and M. S. Rasshchupkyna, *Computational Materials Science: Surfaces, Interfaces, Crystallization* (Elsevier, London, 2013).
[53] P. H. Berens, D. H. J. Mackay, G. M. White, and K. R. Wilson, J. Chem. Phys. **79**, 2375 (1983).
[54] A. Togo and I. Tanaka, Scr. Mater. **108**, 1 (2015).
[55] E. Sanville, S. D. Kenny, R. Smith, and G. Henkelman, J. Comput. Chem. **28**, 899 (2007).
[56] W. Tang, E. Sanville, and G. Henkelman, J. Phys.: Condens. Matter **21**, 084204 (2009).
[57] M. Yu and D. R. Trinkle, J. Chem. Phys. **134**, 064111 (2011).